Volume of Fluid method for low-Mach-number compressible supercritical liquid jet

Jordi Poblador-Ibanez*, William A. Sirignano
Dept. of Mechanical and Aerospace Engineering, University of California, Irvine, CA, USA
*Corresponding author email: poblador@uci.edu

Abstract

A two-phase, low-Mach-number compressible flow solver is proposed. Density variations are linked to changes in composition and temperature rather than pressure. The interface is tracked using a split Volume-of-Fluid method generalized for the case where the liquid velocity is not divergence-free and both phases exchange mass across the interface. A sharp interface is maintained by using a Piecewise Linear Interface Construction (PLIC). At supercritical pressures, the dissolution of lighter gas species into the liquid phase is enhanced and vaporization or condensation can happen simultaneously in different locations along the interface. Mass is conserved to machine-error precision in the limit of incompressible liquid.

The numerical cost of solving two-phase supercritical flows increases substantially because: a) a thermodynamic model is used to determine fluid properties; b) local phase equilibrium and jump conditions are solved together at each interface cell; and c) phase-wise values for certain variables (e.g., velocity) are obtained via extrapolation techniques. To alleviate the increase in numerical cost, the pressure Poisson equation (PPE) is split into a constant coefficient part (implicit) and a variable coefficient part (explicit) and solved using a Fast Fourier Transform (FFT) method. Various tests at high pressures are performed to show the accuracy and viability of the present approach: one-dimensional unsteady flow, two-dimensional capillary wave and planar jet.

Keywords

volume-of-fluid; low-Mach-number compressible flow; supercritical pressure; phase change; phase equilibrium

Introduction

Combustion chambers of many engineering applications operate at elevated pressures. High-pressure chambers improve combustion efficiency and energy conversion per unit mass of fuel. Operating pressures between 25-40 bar can be found in gas turbines, whereas rocket engines can reach 70 to 200 bar. In these applications, liquid fuels based on hydrocarbons are used whose critical pressures are in the range of 20 bar (e.g., Jet-A or RP-1). Understanding how these fuels atomize, vaporize and mix with the oxidizer (e.g., air) is crucial for a proper design of the combustion chamber. At low pressures, the liquid injection problem can be well-analyzed, both experimentally and numerically, due to the simpler thermodynamic environment. However, this is not the case at trans- or supercritical pressures for the liquid fuel, where a thermodynamic transition occurs and the liquid and gas cannot be easily identified [1].

This behavior has often been described as a very fast transition of the liquid phase to a supercritical gas-like state. But evidence of a two-phase behavior exists, whereby the liquid-gas interface must be in local thermodynamic equilibrium (LTE) [2, 3, 4]. The failure to properly identify the two-phase problem in experimental setups is consistent with a fast atomization caused by the extreme thermodynamic environment. Enhanced mixing causes both phases to look more alike near the interface, with reduced surface tension forces and gas-like liquid viscosities [5]. Moreover, fluid properties vary strongly across mixing regions. Thus, traditional imaging-based experimental techniques fail in capturing a liquid core possibly surrounded by a cloud of very small droplets and submerged in a variable-density layer.

The modeling of supercritical two-phase flows is a challenge to the scientific community due to its intrinsic complexity: the non-ideal fluid behavior must be captured, the discontinuous liquid-gas interface is at LTE while both phases exchange heat and mass, the interface must be accurately tracked and a degree of computational efficiency is needed to mitigate the additional computational costs related to the modeling of this thermodynamic environment.

Volume-of-Fluid (VOF) methods are good starting points to develop numerical tools to analyze supercritical liquid injection. A sharp interface is maintained, both during the interface tracking and when solving the governing equations. Additionally, VOF methods handle vaporization or condensation naturally. In this work, the mass-conserving, incompressible VOF method from Baraldi et al. [6] is extended to low-Mach-number compressible two-phase flows coupled with a real-gas thermodynamic model. Moreover, a pressure-correction method based on a split pressure-gradient approach is used, which converts the PPE to a constant-coefficient Poisson equation that can be solved using a computationally-efficient FFT algorithm [7, 8]. The effect of pressure variations on the density is neglected. Thus, density changes are only linked to variations in composition and temperature.

The authors acknowledge the existence of other methods to solve compressible two-phase flows. However, they often present costly and complex interface tracking algorithms, which is a critical issue when simulating supercritical two-phase flows.

Governing equations and thermodynamic model

The low-Mach-number governing equations for supercritical two-phase flows are the continuity and momentum equations, Eq. (1), and the species continuity and energy equations, Eq. (2), expressed in non-conservative form. For simplicity, the real fluid is assumed to be a Newtonian fluid under Stokes' hypothesis. This work considers binary configurations. Thus, only the conservation equation for the mass fraction of a single species (i.e., Y_1) is needed. Mass diffusion is modeled with a high-pressure, mass-based Fickian diffusion coefficient, D_m, and the energy equation is expressed in terms of an enthalpy transport equation.

$$\frac{\partial \rho}{\partial t} + \nabla \cdot (\rho \vec{u}) = 0 \quad ; \quad \frac{\partial}{\partial t}(\rho \vec{u}) + \nabla \cdot (\rho \vec{u} \vec{u}) = -\nabla p + \nabla \cdot \left(\mu \left(\nabla \vec{u} + \nabla \vec{u}^{\mathsf{T}} - \frac{2}{3}(\nabla \cdot \vec{u})\bar{\bar{I}} \right) \right) \quad (1)$$

$$\frac{DY_1}{Dt} = \frac{1}{\rho}\left[\nabla \cdot (\rho D_m \nabla Y_1) \right] \quad ; \quad \frac{Dh}{Dt} = \frac{1}{\rho}\left[\nabla \cdot \left(\frac{\lambda}{c_p}\nabla h \right) + \sum_{i=1}^{N=2} \nabla \cdot \left(\left[\rho D_m - \frac{\lambda}{c_p} \right] h_i \nabla Y_i \right) \right] \quad (2)$$

A thermodynamic model based on a volume-corrected Soave-Redlich-Kwong equation of state (SRK EoS) [9] is implemented. The SRK EoS is able to represent non-ideal fluid states for both phases. Information about how to obtain thermodynamic properties from the SRK EoS, as well as high-pressure correlations to obtain transport properties, is found in Davis et al. [3].

Jump conditions for each governing equation are defined at the interface and are coupled to LTE [10], which is expressed in terms of an equality in fugacity of each species on both sides of the interface. For non-confined, low-Mach-number flows, the thermodynamic pressure is assumed to remain uniform and equal to the ambient pressure. Therefore, fluid properties and transport properties are decoupled from the dynamic pressure responsible for fluid motion.

In this work, the interface is treated as a discontinuity with negligible thickness. Temperature is assumed continuous, although temperature gradients differ on both sides of the interface. The assumptions presented here in modeling the interface are plausible as long as the interface temperature is far away from the mixture critical temperature [11, 12] and the interface thermal resistivity is negligible [13]. The solution of the matching system of equations given by jump conditions and LTE provides the interface temperature, composition and net fluxes per unit area across the interface for mass, momentum, energy and species mass.

Interface tracking

The incompressible and mass-conserving VOF method from Baraldi et al. [6] is extended to address the advection of compressible liquids with phase change. The advection equation for the liquid indicator function, χ where $\chi = 1$ in the liquid and $\chi = 0$ in the gas, is integrated in space over the cell volume and in time with a first-order forward Euler scheme to obtain an equation for the volume fraction, C (see Eq. (3)).

$$\frac{\partial \chi}{\partial t} + \nabla \cdot (\chi \vec{u}_l) = \chi \nabla \cdot \vec{u}_l - \frac{\dot{m}}{\rho_l} \rightarrow C^{n+1} = C^n - \sum_{i=1}^{N_{\text{faces}}} F_i + \tilde{C}(\nabla \cdot \vec{u}_l)\Delta t - \frac{\dot{m}}{\rho_l}\Delta t \qquad (3)$$

The liquid phase is advected by a phase-wise liquid velocity, $\vec{u}_l$. Because of the different fluid compressibilities and the velocity jump across the interface caused by mass exchange, a representative velocity of the liquid phase must be used. ρ_l is the interface liquid density and $\dot{m}$ is the mass flux per unit volume added because of condensation ($\dot{m} < 0$) or subtracted when the liquid vaporizes ($\dot{m} > 0$). It relates to the mass flux per unit interface area, $\dot{m}'$, as $\dot{m} = \dot{m}'\delta_\Gamma$, where δ_Γ is the interfacial surface area density. The term $\sum_{i=1}^{N_{\text{faces}}} F_i$ accounts for the sum of the signed geometrical fluxes of C. Lastly, $\tilde{C}$ is the volume fraction of the cell and only the choice $\tilde{C} = C^{n+1}$ provides a consistent advection. In summary, Eq. (3) represents the change in C at a given cell caused by inflow and outflow of liquid volume fluxes, local volume change of the liquid phase and the volume of liquid added/subtracted due to phase change.

Eq. (3) is solved with a modified Eulerian Implicit (EI), Eulerian Algebraic (EA) and Lagrangian Explicit (LE) split advection algorithm [10]. The first step accounts for mass exchange, followed by the three EI-EA-LE steps and a final correction step to match the form of Eq. (3). The EA step is only needed for three-dimensional flows. The interface is geometrically defined between each step using the PLIC by Youngs [14]. The interface normal unit vector is evaluated using the Mixed-Youngs-Centered method [15] while curvature is computed using an improved Height Function (HF) method [16].

The advection algorithm described here relies on a volume-preserving scheme. Therefore, mass is not conserved to machine error in compressible liquids due to the finite resolution of the liquid density field. However, mesh refinement, both spatial and temporal, improves the mass-conserving properties of the method. In the limit of incompressible liquid without phase change, the present algorithm recovers the approach from [6].

Numerical methods

The main algorithm to solve each time step is presented here in order. Starting from the initial conditions or the previous time step solution, the first step is to advect the interface using the compressible VOF method and evaluate its geometry.

The second step consists in solving the equations for the species mass fraction and mixture enthalpy, Eq. (2). A finite-difference method is used to solve the non-conservative form, where the location of the interface and its solution are embedded in the discretization [10]. Each phase is solved separately. Thus, phase-wise velocities and phase-wise fluid properties are used. The equations are integrated in time with an explicit first-order step and the convective term is discretized using an adaptive first-/second-order upwinding scheme, which provides numerical stability and boundedness (i.e., $Y_1 \leq 1$). The diffusive term is discretized using second-order central differences. However, the inclusion of the interface in the numerical stencil may cause the spatial accuracy to drop between first- and second-order near the interface.

After solving Eq. (2), the third step updates the fluid properties everywhere using the SRK EoS thermodynamic model. Moreover, the jump conditions and LTE are solved at each interface cell. To do so, the normal-probe technique is implemented. A probe perpendicular to the interface is extended into each phase and the values of Y_1 and h are interpolated at different locations on the probe. Then, their gradients perpendicular to the interface can be estimated, which are

needed to determine mass and energy fluxes into the interface. After this step, a full definition of the interface is available (i.e., mixture properties on both sides and geometry).

The fourth step evaluates the fluid compressibilities in both phases and their extrapolation across the interface, as well as the extrapolation of the corresponding phase-wise velocities. The phase-wise values of these terms are only required in a narrow band of cells around the interface for the advection of C and for the discretization of the governing equations. Fluid compressibilities (i.e., $\nabla \cdot \vec{u} = -(1/\rho)(D\rho/Dt)$) are evaluated in non-interface cells using the thermodynamic model as

$$\nabla \cdot \vec{u}^{n+1} = \frac{1}{c_p \bar{v}} \frac{\partial \bar{v}}{\partial T}\bigg|_{Y_i} \frac{Dh}{Dt}^{n+1} + \left[\frac{\rho}{W_1} \frac{\partial \bar{v}}{\partial X_1}\bigg|_{T,X_{j \neq i}} - \frac{\rho}{W_2} \frac{\partial \bar{v}}{\partial X_2}\bigg|_{T,X_{j \neq i}} - \frac{h_1 - h_2}{c_p \bar{v}} \frac{\partial \bar{v}}{\partial T}\bigg|_{Y_i} \right] \frac{DY_1}{Dt}^{n+1} \quad (4)$$

where the various thermodynamic derivatives are evaluated at constant pressure at t^{n+1} as shown in [3] and $(DY_1/Dt)^{n+1}$ and $(Dh/Dt)^{n+1}$ are obtained from the numerical discretization of Eq. (2). $\bar{v}$ is the mixture molar volume and W_1 and W_2 are the molecular weights of each species. Then, the extrapolation techniques by Aslam [17] are adapted to VOF methods and used to extrapolate $\nabla \cdot \vec{u}_l^{n+1}$ and $\nabla \cdot \vec{u}_g^{n+1}$ from each respective phase across the interface. A linear extrapolation is preferred, however a constant extrapolation might be required for numerical stability. Once the phase-wise velocity divergences have been extrapolated, the phase-wise velocities are obtained by extending the extrapolation equation from Dodd et al. [8] to compressible flows. Eq. (5) represents the extrapolation of the liquid phase-wise velocity, $\vec{u}_l$, solved directly at steady-state to match the previously extrapolated liquid velocity divergence, defined as g. Here, τ acts as a pseudotime, which does not have units of time. $\vec{u}_g$ is obtained in a similar manner.

$$\frac{\partial \vec{u}_l}{\partial \tau} + \nabla(\nabla \cdot \vec{u}_l) = \nabla g \rightarrow \nabla(\nabla \cdot \vec{u}_l) = \nabla g \quad (5)$$

Finally, the fifth step solves the momentum equation subject to the continuity constraint. Contrary to the approach used in the resolution of Eq. (2), here Eq. (1) is solved in conservative form using the finite-volume method. A one-fluid method is used where fluid properties are volume-averaged at the interface cells and the jump conditions are modeled through localized source terms in the momentum and continuity equations. A sharp interface is maintained since both the volume averaging and the activation of interfacial source terms occurs within a region of $\mathcal{O}(\Delta x)$. The one-fluid momentum equation reads

$$\frac{\partial}{\partial t}(\rho \vec{u}) + \nabla \cdot (\rho \vec{u}\vec{u}) = -\nabla p + \nabla \cdot \left(\mu \left(\nabla \vec{u} + \nabla \vec{u}^{\mathsf{T}} - \frac{2}{3}(\nabla \cdot \vec{u})\bar{\bar{I}} \right) \right) + \frac{\rho}{\langle \rho \rangle} \left(\sigma \kappa \nabla C + \nabla_s \sigma |\nabla C| \right) \quad (6)$$

where the momentum jump due to surface tension forces is included as a source term using the Continuum Surface Force approach applied to variable surface-tension fluids [18].

The momentum equation is solved explicitly using a first-order time integration and a predictor-projection method. The convective term is discretized using the SMART algorithm and the one-fluid velocity (i.e., the velocity directly provided by the solution of the momentum equation). Near the interface, a hybrid method is used that combines second-order central differences with a first-order upwind scheme. On the other hand, the viscous term is discretized with second-order central differences using the phase-wise velocity to avoid artificial pressure spikes [8].

A constant-coefficient PPE is built using the split pressure-gradient method for two-phase flows [7, 8] to obtain the pressure field and the one-fluid velocity that satisfies the continuity equation as

$$\nabla^2 p^{n+1} = \nabla \cdot \left[\left(1 - \frac{\rho_0}{\rho^{n+1}} \right) \nabla \hat{p} \right] + \frac{\rho_0}{\Delta t} \left(\nabla \cdot \vec{u}^p - \nabla \cdot \vec{u}^{n+1} \right) \quad (7)$$

where $\vec{u}^p$ is the velocity obtained in the predictor step, ρ_0 is the smallest fluid density (i.e., pure gas density) and $\hat{p} = 2p^n - p^{n-1}$ is an explicit linear extrapolation in time of the pressure field. Following Duret et al. [19], the one-fluid continuity constraint is estimated as

$$\nabla \cdot \vec{u}^{n+1} = -(1-C)\frac{1}{\rho_g}\frac{D\rho_g}{Dt} - C\frac{1}{\rho_l}\frac{D\rho_l}{Dt} + \dot{m}\left(\frac{1}{\rho_g} - \frac{1}{\rho_l}\right) \tag{8}$$

with all terms evaluated at time t^{n+1}. Because Eq. (7) has constant coefficients, it can be solved using a FFT method [7]. This approach saves computational time usually spent in solving the PPE. Therefore, computational resources can be redirected towards solving the expensive algorithm steps added in supercritical two-phase problems: the use of a real-gas thermodynamic model, the solution of a system of equations at each interface cell to determine the interface properties and the extrapolation of phase-wise velocity divergences and their corresponding velocities. Further details on this numerical approach are available in [10].

Results and discussion

The supercritical two-phase solver proposed here is validated against different test cases. Due to the intrinsic complexity of the problem, no analytical solutions are available and the focus is on the numerical behavior and the qualitative correctness of the observed physics. A more detailed analysis is presented in [10]. In all test cases, the liquid phase is initially composed of *n*-decane at 450 K and the gas phase is composed of oxygen at 550 K.

A one-dimensional configuration where an unperturbed liquid pool is sitting on a wall is analyzed. The qualitative behavior is in good agreement with [2], yet here the thermodynamic model has been improved, the interface is allowed to move and the momentum equation is solved. As the sharp initial condition relaxes, mass and heat diffuse in both phases. Higher pressures enhance the dissolution of oxygen in the liquid phase and cause stronger variations in fluid properties across the mixing region.

The direction of the interface displacement also matches the displacement predicted in [2]. At 10 bar, vaporization reduces the liquid volume (i.e., the interface recedes). Even though at 50 bar the interface is vaporizing, there is enough dissolution of oxygen into the liquid as to locally expand the liquid volume. Thus, the liquid volume increases. At 100 and 150 bar, both local volume expansion and condensation contribute to the increase in liquid volume.
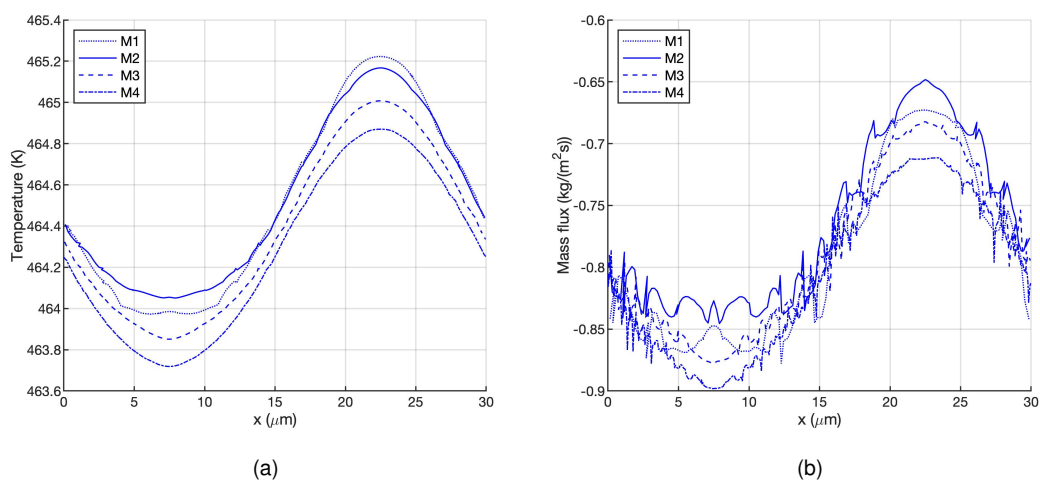

Figure 1. Two-dimensional capillary wave: Mesh convergence of the interface solution at $t = 19\ \mu$s for the 150-bar case. (a) temperature; (b) net mass flux.

A two-dimensional capillary wave is also analyzed. Both phases are initially at rest and with the same mixture composition and temperature as in the one-dimensional test. Here, the interface is initially perturbed with a sinusoidal wave of 30 μm wavelength and 1 μm amplitude. The

interface amplitude will relax in time and the overall solution will tend to a one-dimensional behavior similar to the previous test. However, this problem lets us analyze mesh convergence of the interface solution and mass conservation, as well as show some of the features of supercritical two-phase flows, for deformed interfaces.

Figure 1 shows the mesh convergence of the interface temperature and mass flux at $t = 19$ μs for the 150-bar case. Four different uniform meshes are analyzed: M1 (0.3 μm), M2 (0.2 μm), M3 (0.1 μm) and M4 (0.05 μm). The mixing around the interface can be captured better for finer meshes. The concentration and enthalpy gradients obtained with normal-probe technique are more accurate and a smoother sinusoidal distribution of interface properties is obtained (Figure 1a). As in the one-dimensional case, net condensation occurs along the interface. Similar to the oscillations in curvature caused by the HF method, the mass flux solution is very sensitive to the non-smoothness of the interface and mixing region around it. Thus, some numerical oscillations are observed (Figure 1b). Overall, first-order or lower spatial convergence rates are observed for the interface properties. Even though one-dimensional interfaces show a better behavior, it is not surprising that the complexity of the model causes two- and three-dimensional interfaces to show limited spatial convergence. This issue has been reported in other works as well [20]. Nevertheless, the normalized errors between two consecutive meshes are of the order of 1% or less. On the other hand, the interface dynamics present a better spatial convergence and are little affected by the small variations in interface properties. Figure 2a shows the temporal relaxation of the interface amplitude at the initial wave crest location ($x = 7.5$ μm) at 150 bar obtained with the four different meshes.

Mass errors are evaluated by comparing the normalized difference between the liquid mass at a given time and the initial liquid mass with the accumulated mass exchanged across the interface. Both approaches should be equivalent, but the resolution of the density field and the accuracy to which the mass flux across the interface is obtained cause some differences. Mesh refinement improves mass conservation, with the error dropping to 1% for mesh M4.
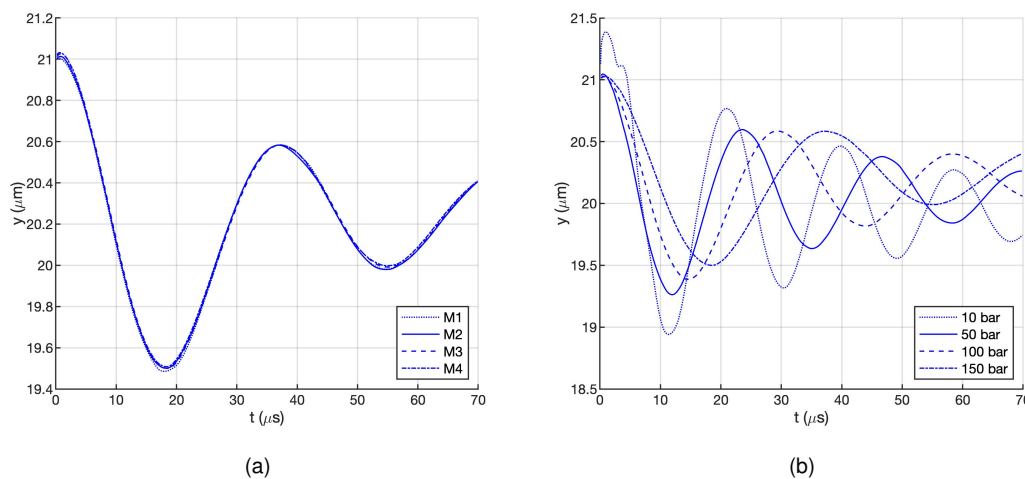

Figure 2. Two-dimensional capillary wave: Interface amplitude relaxation vs. time at the initial wave crest location of $x = 7.5$ μm. (a) mesh convergence at 150 bar; (b) various pressures with M3.

Some pressure effects on the interface dynamics are seen in Figure 2b. The relaxation of the interface amplitude at $x = 7.5$ μm is shown for different pressures. A drift towards higher y values caused by enhanced liquid volume expansion and condensation is observed as pressure increases. A similar perturbation damping occurs for all pressures; however the reduction in surface tension forces as pressure increases causes the oscillation frequency to drop.

The last test demonstrates the ability of the numerical model to capture the interface deformation seen in liquid injection, as well as the relevant physics at supercritical pressures. A symmetric two-dimensional temporal planar jet with a half thickness of 10 μm is initially perturbed with a

sinusoidal wave of 30 μm wavelength and 0.5 μm amplitude. The ambient pressure is 150 bar and a thin streamwise velocity distribution is imposed around the interface, varying from 0 in the liquid phase to 30 m/s in the gas phase following a hyperbolic tangent profile. Periodicity is imposed in the streamwise direction and outflow boundary conditions are imposed in the gas phase top boundary.
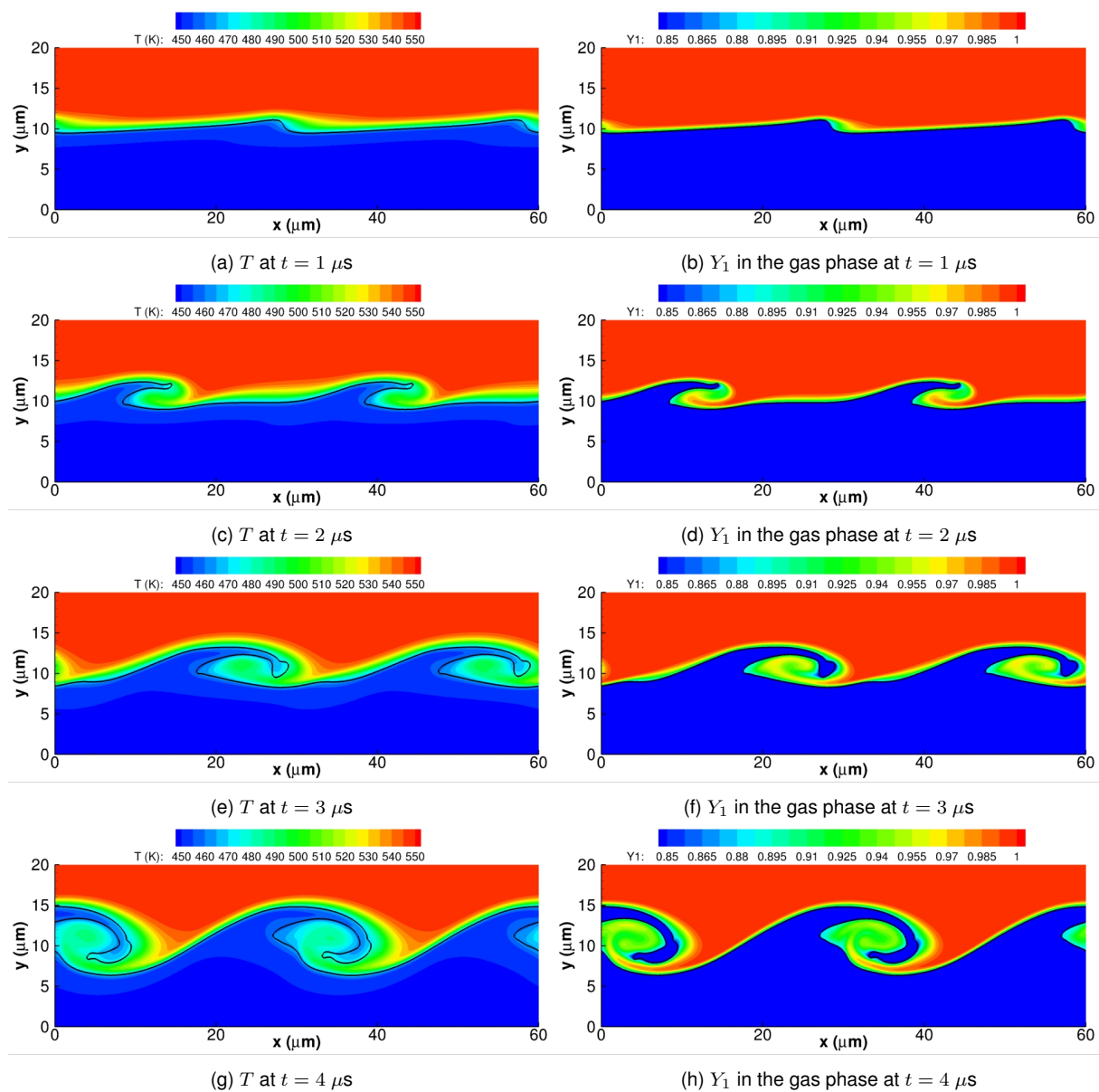

(a) T at $t = 1$ μs

(b) Y_1 in the gas phase at $t = 1$ μs

(c) T at $t = 2$ μs

(d) Y_1 in the gas phase at $t = 2$ μs

(e) T at $t = 3$ μs

(f) Y_1 in the gas phase at $t = 3$ μs

(g) T at $t = 4$ μs

(h) Y_1 in the gas phase at $t = 4$ μs

Figure 3. Two-dimensional planar jet: Temperature distribution and Y_1 distribution in the gas phase at 150 bar with M4. The interface location is highlighted with a solid black curve.

Figure 3 shows the distributions of temperature and oxygen mass fraction, Y_1, as well as the interface deformation, at different times. The characteristics of the mixing process can be seen where the swirling motion captures regions of hotter gas and higher oxygen concentration into the liquid structure. Moreover, the fast growth of the surface instability at high pressures is apparent and similar to that reported in [5], which can be linked to a faster atomization.

Other interesting results not shown here related to mixing in the liquid phase. The elongated liquid region presents lower densities and gas-like viscosities, which contribute to a faster deformation under the effects of the shear forces caused by the faster gas.

Conclusions

The viability and accuracy of the numerical model presented in this work to address two-phase supercritical flows has been demonstrated. The low-Mach-number governing equations for two-phase flows are coupled to a non-ideal thermodynamic model and a VOF method for compressible liquids with phase change. Extra computational costs are added to the algorithm because of the extrapolations of phase-wise values or the solution of the jump conditions and LTE at every interface cell. To mitigate them, a constant-coefficient PPE is used, which can be solved with a FFT method. Future work includes three-dimensional results of planar jets, the analysis of the role of vortex dynamics in the deformation of the liquid and a thermodynamic characterization of the interface (e.g., identify regions of condensation/vaporization).

Acknowledgments

References

[1] Mayer, W.O.H., Schik, A.H.A., Vielle, B., Chauveau, C., Gökalp, I., Talley, D.G., Woodward, R.D., 1998, *Journal of Propulsion and Power*, 14 (5), pp. 835-842.

[2] Poblador-Ibanez, J., Sirignano, W.A., 2018, *International Journal of Heat and Mass Transfer*, 126, pp. 457-473.

[3] Davis, B.W., Poblador-Ibanez, J., Sirignano, W.A., 2021, *International Journal of Heat and Mass Transfer*, 167, pp. 120687.

[4] Poblador-Ibanez, J., Davis, B.W., Sirignano, W.A., 2021, *International Journal of Multiphase Flow*, 135, pp. 103465.

[5] Poblador-Ibanez, J., Sirignano, W.A., May 2019, ILASS-Americas 30th Annual Conference on Liquid Atomization and Spray Systems.

[6] Baraldi, A., Dodd, M., Ferrante, A., 2014, *Computers & Fluids*, 96, pp. 322-337.

[7] Dodd, M., Ferrante, A., 2014, *Journal of Computational Physics*, 273, pp. 416-434.

[8] Dodd, M., Trefftz-Posada, P., Ferrante, A., 2021, *In Preparation*

[9] Lin, H., Duan, Y.-Y., Zhang, T., Huang, Z.-M., 2006, *Industrial & Engineering Chemistry Research*, 45 (5), pp. 1829-1839.

[10] Poblador-Ibanez, J., Sirignano, W.A., 2021, *Under Review. Available at arXiv.org eprint: 2103.01874*

[11] Dahms, R.N., Oefelein, J.C., 2013, *Physics of Fluids*, 25 (9), pp. 092103.

[12] Dahms, R.N., Oefelein, J.C., 2015, *Proceedings of the Combustion Institute*, 35 (2), pp. 1587-1594.

[13] Stierle, R., Waibel, C., Gross, J.,Steinhausen, C., Weigand, B., Lamanna, G., 2020, *International Journal of Heat and Mass Transfer*, 151, pp. 119450.

[14] Youngs, D.L., 1982, *Numerical Methods for Fluid Dynamics*, 1, pp. 41-51.

[15] Aulisa, E., Manservisi, S., Scardovelli, R., Zaleski S., 2007, *Journal of Computational Physics*, 225 (2), pp. 2301-2319.

[16] López, J., Zanzi, C., Gómez, P., Zamora, R., Faura, F., Hernández, J., 2009, *Computer Methods in Applied Mechanics and Engineering*, 198 (33-36), pp. 2555-2564.

[17] Aslam, T.D., 2004, *Journal of Computational Physics*, 193 (1), pp. 349-355.

[18] Seric, I., Afkhami, S., Kondic, L., 2018, *Journal of Computational Physics*, 352, pp. 615-636.

[19] Duret, B., Canu, R., Reveillon, J., Demoulin, F., 2018, *International Journal of Multiphase Flow*, 108, pp. 42-50.

[20] Palmore Jr, J., Desjardins, O., 2019, *Journal of Computational Physics*, 399, pp. 108954.